Modeling and optimization of debris mitigation systems for laser and discharge-produced plasma in extreme ultraviolet lithography devices

Valeryi Sizyuk
Ahmed Hassanein
Argonne National Laboratory
9700 South Cass Avenue, Building 308
Argonne, Illinois 60439
E-mail: sizyuk@anl.gov

Vivek Bakshi
SEMATECH Corporation
2706 Montopolis Drive
Austin, Texas 78741

Abstract. Physical models are developed to investigate the following conditions relevant to discharge-produced plasma (DPP) devices under development for extreme ultraviolet (EUV) lithography: gaseous jet propagation in the chamber, removal of neutral particles with a gaseous jet, and deviation of charged particles with a magnetic field. Several geometries of the mitigation systems are considered for removing debris during the EUV lithographic process. The design of a mitigation system is proposed and simulated with the computer models. The behavior of Xe, Li, and Sn debris in Ar and He jets is simulated by using the high energy interaction with general heterogeneous target systems (HEIGHTS) integrated package. Final energy and local distributions are calculated using experimental debris data from current EUV facilities.
 [DOI: 10.1117/1.2804128]

Subject terms: debris mitigation; laser-produced plasma; discharge-produced plasma; lithography; numerical simulation; Monte Carlo method.

Paper 06097RR received Dec. 15, 2006; revised manuscript received Jul. 16, 2007; accepted for publication Jul. 26, 2007; published online Nov. 2, 2007.

1 Introduction

Discharge-produced plasma (DPP) devices have been proposed as a light source for extreme ultraviolet (EUV) lithography. A key challenge for DPP is achieving sufficient brightness to support the throughput requirements of exposure tools for high-volume manufacturing lithography. To simulate the environment of the EUV source and optimize its output, we are developing an integrated model[1–4] that will describe the hydrodynamics and optical processes that occur in DPP devices. Various methods of fuel delivery and discharge regimes have been investigated using the high energy interaction with general heterogeneous target systems (HEIGHTS) integrated models. These models include utility programs for calculating EUV output and optimizing the reflection system geometry.

Another important problem is the lifetime of the source components, in particular, that of the collector mirror reflectivity. The collector mirror lifetime is a major issue for discharge- and laser-produced plasma sources, where multilayer as well as single layer mirrors are used as collector systems. The collector optic lifetime noticeably decreases under the influence of plasma device debris: droplets, neutral particles, and accelerated ions.[5,6] As a result, the EUV lithography community is actively investigating methods of debris mitigation.

This work describes the physical models developed for simulating and optimizing a debris mitigation device based on gaseous jets and external magnetic fields. The proposed debris mitigation system includes a gaseous pipe jet for removing neutral debris and a deflecting magnetic field for deviating fast ions.

1537-1646/2007/$25.00 © 2007 SPIE

2 Mathematical Model

The main parts of the proposed mitigation system described in this work are a gaseous jet in a chamber and an external magnetic field. Because the EUV source device has two sorts of debris (neutral droplets and accelerated ions), the theoretical models developed to fully describe the mitigation system incorporate the hydrodynamics of the gaseous jets in the chamber, neutral droplet deceleration and deviation in the gaseous jet, and fast-ion interaction with gaseous matter in the external magnetic field. Physical and mathematical models were developed for the gaseous motion in EUV devices. These models were used to develop the 2-D numerical HEIGHTS-JET package. This package solves the general set of hydrodynamic equations using the conservation laws of mass density, momentum, and energy for 2-D cylindrical symmetry,

$$\begin{aligned}
&\frac{\partial \rho}{\partial t} + \frac{1}{r}\frac{\partial}{\partial r}(r\rho V_r) + \frac{\partial}{\partial z}(\rho V_z) = 0,\\
&\frac{\partial \rho V_r}{\partial t} + \frac{1}{r}\frac{\partial}{\partial r}(r\rho V_r V_r) + \frac{\partial p}{\partial r} + \frac{\partial}{\partial z}(\rho V_r V_z) = 0,\\
&\frac{\partial \rho V_z}{\partial t} + \frac{1}{r}\frac{\partial}{\partial r}(r\rho V_r V_z) + \frac{\partial}{\partial z}(\rho V_z V_z + p) = 0,\\
&\frac{\partial e_t}{\partial t} + \frac{1}{r}\frac{\partial}{\partial r}(rV_r[p + e_t]) + \frac{\partial}{\partial z}(V_z[p + e_t]) = 0,
\end{aligned} \tag{1}$$

where ρ is the density of gas; and V_r and V_z are velocity components; p is the pressure of gas; and e_t is the total energy density of gas. Equation (1) is closed with approxi-

mated gas properties for a temperature of ~500 K,

$$e_t = e_i + e_k = \frac{\rho RT}{\mu(\gamma-1)} + \frac{\rho(V_r^2+V_z^2)}{2},$$

$$p = e_i(\gamma-1) = \frac{\rho RT}{\mu}, \tag{2}$$

$$V_{ac} = \sqrt{\frac{\gamma p}{\rho}}.$$

Here, e_i is the internal energy; e_k is kinetic energy; T is temperature; R is the gas constant; μ is the molar mass; V_{ac} is the speed of sound; and γ is an adiabatic constant.

Equation (1) was solved by the total variation diminishing (TVD) method as described in Refs. 1 through 4. The final results include the density and velocity fields of the chamber gas (He or Ar) by organizing the gaseous flow around the debris source. We analyzed several constructions of nozzles for a stable flow. Also, the effects of flow rate and pressure magnitude were calculated for the working gases Ar and He.

Hydrodynamic calculations of the density and velocity fields were used as initial data to consider droplet behavior in the jet stream. The equation of motion is given for spherical droplets as

$$m_d \frac{d\mathbf{V}_d}{dt} = -\psi \frac{\rho_g |\mathbf{V}_d - \mathbf{V}_g| \cdot (\mathbf{V}_d - \mathbf{V}_g)}{2} \pi r_d^2, \tag{3}$$

where m_d is the droplet mass, $\mathbf{V}_d$ is the droplet velocity, $\mathbf{V}_g$ is the gas velocity, and r_d is the droplet radius. The drag coefficient ψ was calculated in the Schiller-Nauman form:

$$\psi = \frac{24}{\mathrm{Re}} + \frac{4}{\sqrt[3]{\mathrm{Re}}}, \tag{4}$$

with Reynolds number

$$\mathrm{Re} = \frac{2 r_d \rho_g [(V_d^r - V_g^r)^2 + (V_d^z - V_g^z)^2]^{1/2}}{\eta}. \tag{5}$$

The viscosity η of the working gas was calculated using the formula[7]

$$\eta = 0.3502 \frac{(3 k_b T_g m_{gm})^{1/2}}{\pi d_{gm}^2}, \tag{6}$$

for a gas molecule with mass m_{gm} and diameter d_{gm}. Here, k_b is the Boltzmann constant and T_g is the gas temperature.

The Monte Carlo (MC) model was constructed for the initial debris condition. Experimental size, velocity, and direction distributions[8,9] were used for simulating the debris beam. The MC numerical block has two methods for initial distribution sampling: approximation with analytical functions and direct MC sampling. The Nukiyama-Tanasawa distribution[10] is used for sampling debris size in the beam

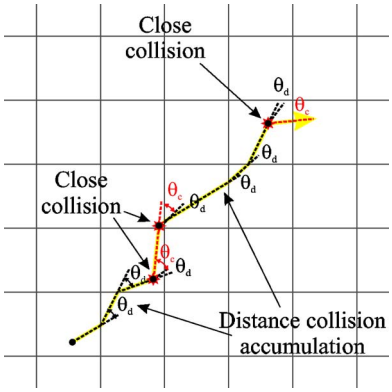

Fig. 1 Monte Carlo model of ion collisions.

$$f(r_d) = a(r_d)^2 \exp\{-b(r_d)^x\}, \tag{7}$$

where r_d is the droplet radius. The initial velocity distributions of particles were also directly obtained from the experimental data in a manner similar to the size distribution method. The theoretical[10] and experimental[8,9] distribution were sampled with the patchwork rejection method.[11]

Interaction between separate particles underlies all effects that occur from the interaction of various particles with matter. The physical model that can be used to describe particle penetration through the target should be constructed by considering the separate interactions of beam particles with the target particles. This is the well-known approximation of pair collisions.[12] In this approximation, the bullet particle is assumed to interact simultaneously with only one particle of the target (nucleus or electron). This interaction occurs instantly at one point. Our Monte Carlo model is based on this principle and supposes that bullet particles are remote one from another by a distance larger than the Coulomb shielding in the target. These assumptions allow introducing the concept of the particle trajectory as a line of combined sections between separate interactions (Fig. 1). The energy and pulse of the particle change at the points of interaction. Because the initial energy of the fast ions does not exceed 50 keV, nonelastic scattering is not included. The HEIGHTS models have a more detailed Monte Carlo model of this process. However, it is not possible to take into account all interactions of bullet particles with the target particles separately, because of limited computer abilities. For this reason, all interactions are separated into two groups: close collisions and distant collisions. The criterion for this separation is the energy that is transmitted to the recoiled particle. In the present model, all interactions where bullet particles lose energy less than 10^{-2} from the initial value are considered distant. The distant interaction results accumulate on the trajectory and should be added at the end of the bullet particle path. The Monte Carlo model developed is related to the small energy transfer grouping methods.[13]

In the physical model, fast ions of the EUV source debris can interact with nuclei and electrons in the chamber gas for both distant and close interactions. Initial data for calculations start with the density field of the target gas and the source energy distribution of fast ions. The interactions of fast ions with the chamber gas nuclei were calculated

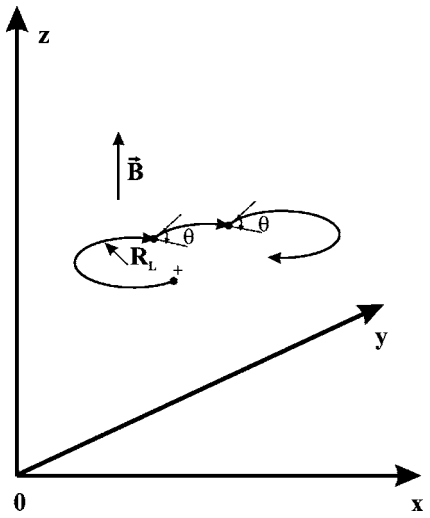

Fig. 2 Scattering scheme of fast ions under external.

with an approximation of the Thomas-Fermi potential. The modeling of distant collisions of fast ions with electrons is more complicated because two approximations must be used for the interaction description:[14] the Bethe theory for high energy of the bullet ions, and the Linhard stopping power for low energy ions. We developed a fitting function for the continuous combining of both models.

On the basis of these theories, we have constructed a Monte Carlo algorithm for calculating fast ion deceleration in the chamber gas. The algorithm takes into account the secondary (recoiled) particles if the energy of these particles is higher than a critical magnitude. This assumption allows the accurate calculation of the energy deposition in the chamber gas. An external magnetic field can be used in fast ion mitigation systems for two purposes: to extend the ion path through damping matter and to redirect ions from the reflection system to a safe location. As a supplement to the constructed Monte Carlo theory, we added the effect of external magnetic field on the free-fly trajectories of a charged particle between scattering (see Fig. 2).

3 Validation and Benchmarking

The most important and new part of the developed physical model and HEIGHTS code is the Monte Carlo block related to the fast ion interactions with the chamber gas. For this reason, HEIGHTS calculations were compared with available experimental and theoretical data for ion energies of 17 keV and 1.2 MeV. In the low-energy case, the energy distribution of the Li^+ ions was calculated for transmission through a 14-nm-thick Cu film.[15] Figure 3 shows the good correspondence between our calculations and experimental data for the 17-keV Li^+ ions.[15] Experimental[16] and theoretical[17] data were also compared for 1.2-MeV P^+ ions implanted into a Si substrate. Figure 4 compares the distributions of the dopant (implantation dose, 1×10^{14} cm^{-2}) derived from the HEIGHTS calculations to the published experimental and numerical data. The presented figures show correspondence of our calculations to the experimental data with reasonable accuracy. The difference in the curve form and the curve maximum location can be explained (by opinion of the Ref. 15 authors and by our opinion) with the uncertainty in the effective bullet ion charge determination. The effective charge uncertainty increases with the ion energy decreasing. With this notation, we interpreted the presented figures as validation of the HEIGHTS theoretical model and integrated numerical scheme for the study of mitigation processes for EUV lithography. Benchmarking of the hydrodynamics part of the code can be found in Ref. 18.

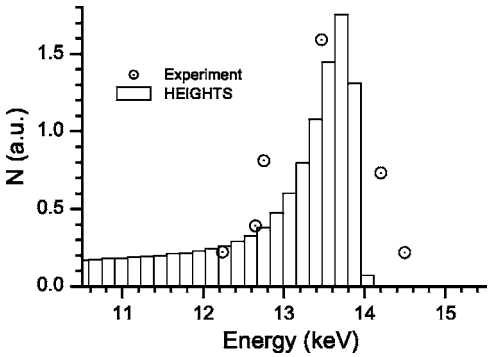

Fig. 3 Comparison of HEIGHTS and experimental[13] energy distributions of the 17-keV Li^+ ions after transmission through 14-nm Cu film.

4 Results and Discussion

To evaluate the working gas density, we calculated the EUV transparency for the main working gas candidates: He and Ar. The EUV flux attenuation was estimated for the diapason $13.5\pm2\%$ with an absorption coefficient data for the neutral gas from Ref. 19.

Figure 5 presents calculated EUV intensity results for a temperature of 500 K and three variants of chamber pressure: 1, 5, and 10 Pa (1×10^{-8}, 5×10^{-8}, and 1×10^{-7} g/cm^3). The horizontal dashed line shows the 10% level of EUV flux used to estimate chamber and mitigator size. As assumed initially, He gas is more transparent for EUV. However, both gases can be used for chamber filling; for the practical pressure magnitude ($\sim$5 Pa, 500 K), the EUV flux loses 10% per meter in Ar and 4% per meter in He. These values are applicable to mitigation device construction.

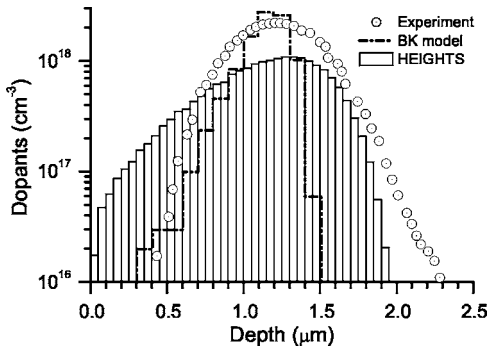

Fig. 4 Comparison of HEIGHTS calculations with experimental[16] and theoretical[17] data. The depth distributions are for P^+ dopant in Si substrate. Initial energy of dopant, 1.2 MeV; implantation dose, 1×10^{14} cm^{-2}.

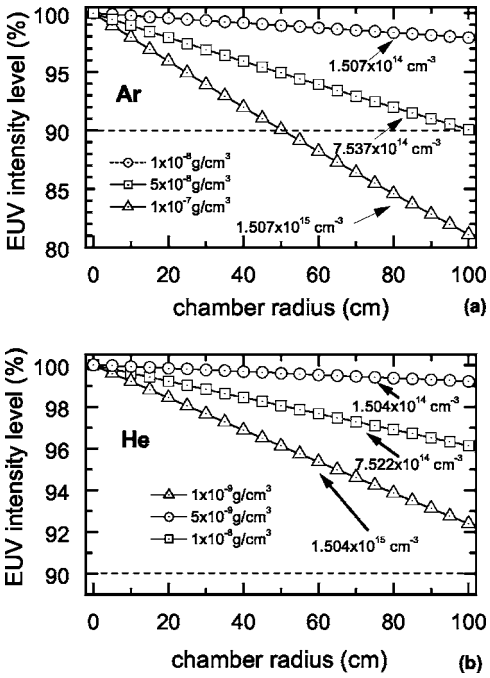

Fig. 5 The transparency of chamber gas for EUV radiation at 500 K for various pressures: (a) Ar gas and (b) He gas.

Before full simulation of the gaseous jet mitigator, we considered the slow down of the spherical droplets in the static chamber gas. Deceleration of the Sn particles was simulated in He gas at the regular chamber pressure of 5 Pa and higher. The final velocity was registered at a distance of 5 cm from the droplet start. Figure 6 shows the critical dependence of deceleration on the droplet size (radius of 1.5, 2.0, and 5.0 μm) for the jet gas pressure where the mean free path of gas molecules is comparable with the neutral droplet size. Droplets with a radius of less than 1 μm would be damped completely. Only large particles would keep significant velocity. This estimation shows that with the gaseous jet mitigator, large particles will be processed to a lesser degree than small debris. For low gas pressures, more detailed analysis is required where the droplet motion in the gas will be collisionless. This work is currently underway.

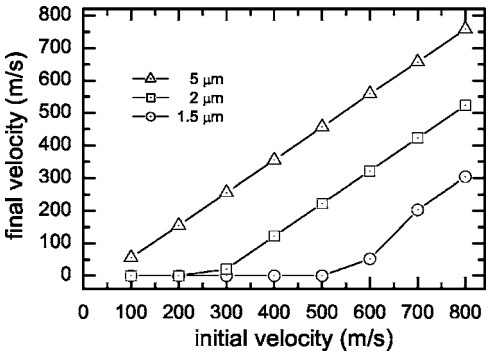

Fig. 6 Deceleration of tin particles having different radii in He gas at a distance of 5 cm.

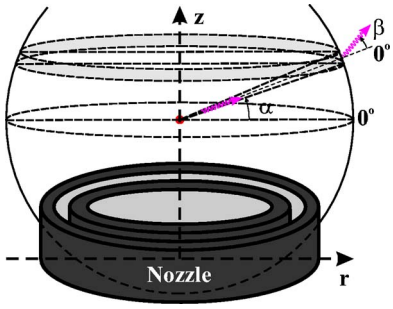

Fig. 7 Debris detector construction: α is the initial aiming angle and β is the deviation angle.

The various geometries of the hollow (pipe) variant of the jet were considered for several geometries of the mitigator device. All geometries were studied to obtain a stable and compact flow expansion in the chamber volume. Testing was done with the two gases (Ar and He) at an initial temperature of 500 K and stream velocity of Mach 1. To calculate the efficiency of debris mitigation, a particle detector was designed. Figure 7 schematically presents the spherical surface used for nonmitigated particle detection. The debris source is on the z axis near the jet convergence point ($z \sim 6$ cm). The radius of the mitigation sphere was variable.

As presented in Fig. 8, the location of the debris source can be used to regulate the motion of the neutral particles. The structure of the curves is defined with the complex structure of the gaseous flow, which includes the z-directed annular flow and the opposite directed central pipe flow. The annular flow collapses at any z distance above the nozzle exit section with initiation of the internal central flow in the opposite (to the nozzle central hole in Fig. 7) direction. The location of the debris source relative the collapse point sets conditions for the debris motion. The angle distribution of Sn droplets also depends on the z coordinate of the source. The initial direction of the debris in this numerical experiment was chosen to be equiprobable. The total number of tested particles was 10^8.

The behavior of the charged particles in the chamber gas was considered separately from that of the neutral particles. Damping capabilities of the chamber gas are important not only for the energy decrease of the mirror bombardment

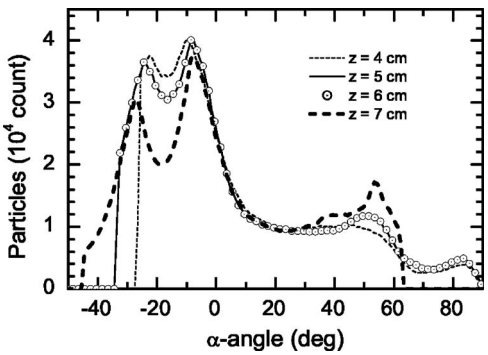

Fig. 8 Mitigation results for different z locations of Sn droplet source. Initial number of particles, 10^8.

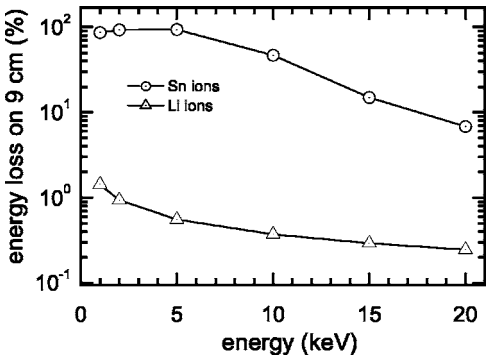

Fig. 9 Energy loss of ions in He jet at a distance of 9 cm. Percentage relative to the initial energy.

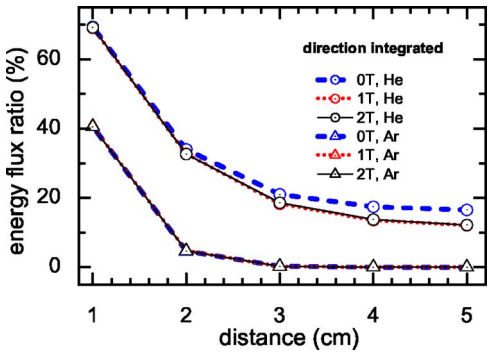

Fig. 11 Decreasing energy flux (integrated by direction) of the Sn ions with distance.

flux, but also for the future magnetic field control of the charged particles. An actual reduction of the ion velocity follows from a decrease of the Larmor radius; as a result, slower particles can be easily deviated to the safe area. We calculated the deceleration of light Li and heavy Sn ions in the He chamber gas in the initial energy range up to 20 keV. It was supposed that heavy ions decelerate more effectively than light ions at the same energy. This supposition is supported by the lower velocity of the heavy ions: slow ions damp more effectively than fast ions. Figure 9 compares percent energy losses of the Li and Sn ions for the distance of 9 cm in the He chamber gas at the regular pressure of 5 Pa. The absolute values of the final energy of the decelerated ions are plotted in Fig. 10 with respect to the initial energy determined from the Sn and Li ion numerical experiment.

The previous results indicate that heavy ions can be decelerated more effectively than light ions. However, in the case of EUV source plasmas, the light ions have less initial energy than heavy ions. It was proposed that a magnetic field be used with the open pipe jet to improve the mitigation of charged particles. Fast ions of Sn were tested as the debris sample. The initial energy distribution of the fast Sn ions was taken from Ref. 5. The start-velocity direction distribution was equiprobable. The total number of the test particles was 10^6. The detector radius was decreased to 5 cm for fast ions.

We investigated the fast-ion energy flux attenuation as a function of the device radius for the gaseous jet case (~5 Pa, He or Ar). Energy flux was integrated by direction.

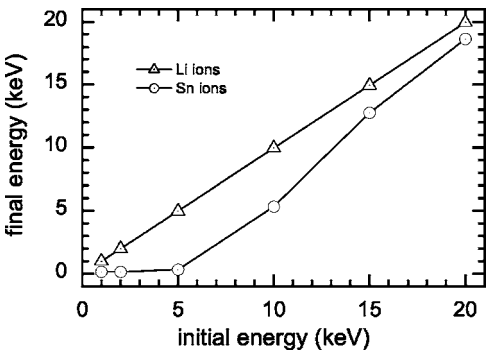

Fig. 10 Ion deceleration in He jet at a distance of 9 cm.

Figure 11 shows the ion energy increasing with distance for three values of the external magnetic field: 0, 1, and 2 T. As shown, the external magnetic field noticeably decreases the ion energy in the He gas case for distances longer than 3 cm. This effect can be explained by a small amount of fast-ion scattering in He and the Larmor radius value being ~2 cm. An increased scattering efficiency (due to the gas density increasing, chamber gas being heavier, etc.) reduces the influence of the magnetic field. The fast-ion deceleration in the chamber gas due to the scattering and the deviation of the ions by the magnetic field are two competitive processes in the mitigation system: if the chamber gas is too rarefied or light in weight, a magnetic field can be applied to compensate for a deficit in the deflecting force. The He curves in Fig. 11 show the deficient debris deviation with gas only for the selected density: the magnetic field influence is significant. In the opposite, the same density for the Ar gas is enough for fast-ion deceleration, and an additional magnetic field is useless. As a consequence, the mitigation system should be optimized for the following plasma source parameters: geometry, size, distance to the reflection system, and working gas properties. A safe location for the decelerated debris can be determined from the directional debris distributions of the mitigation system.

Our theoretical model was developed by assuming that the debris flow is rarefied and cannot change the parameters of the mitigator gaseous jet. To meet the requirements of high-volume manufacturing (HVM), the results should be recalculated for the conditions of high repetition-rate plasma sources. Our previous numerical experiments with laser and discharge produced plasma show a considerable variation in the chamber gas parameters up to ~2 cm from the plasma source during the working cycle. The assumption of the equivalence of the high-frequency operation to the continuous changing of the gas parameters (up to the 2-cm distance) leads to predicted results consistent with those presented in this work for a mitigation system ~5 cm and larger. The data for fast-ion deviation are more accurate than those for the neutral droplet debris, because the ions have a much higher velocity in the chamber gas, and continuous operation of the plasma device slightly modifies the fast-ion deceleration results. We suppose that the continuous operation of the plasma device results in widening of the gaseous pipe jet and the differences in the calculation for neutral debris disposal.

5 Conclusions

Physical models are developed for simulating the main processes that occur in EUV lithography mitigation systems: gaseous jet propagation in the chamber, removal of neutral particles and macroscopic droplets with the gaseous jet, and deviation of charged particles with a magnetic field. Various geometries of the mitigation system are considered for debris removal by the EUV lithographic process. Other mitigation geometries can be easily accommodated. Xe, Li, and Sn debris in Ar and He gaseous jets are analyzed using the developed HEIGHTS-JET simulation package. Attenuation of EUV flux by propagation through a neutral chamber gas is calculated for He and Ar. A 3-D Monte Carlo model of ion propagation in the chamber gas is developed. The initial distributions of fast ions are derived from experimental data. Sn ion mitigation is modeled with and without an external magnetic field.

Acknowledgments

The major part of this work is supported by SEMATECH. Argonne National Laboratory is operated by the University of Chicago for the U.S. Department of Energy under contract W-31-109-Eng-38.

References

1. A. Hassanein, V. Sizyuk, V. Tolkach, V. Morozov, and B. J. Rice, "HEIGHTS initial simulation of discharge-produced plasma hydrodynamics and radiation transport for EUV lithography," *Proc. SPIE* **5037**, 714–727 (2003).
2. A. Hassanein, V. Sizyuk, V. Tolkach, V. Morozov, and B. J. Rice, "HEIGHTS initial simulation of discharge produced plasma hydrodynamics and radiation transport for extreme ultraviolet lithography," *J. Microlithogr., Microfabr., Microsyst.* **3**(1), 130–138 (2004).
3. A. Hassanein, V. Sizyuk, V. Tolkach, V. Morozov, T. Sizyuk, B. J. Rice, and V. Bakshi, "Simulation and optimization of DPP hydrodynamics and radiation transport for EUV lithography devices," *Proc. SPIE* **5374**, 413–422 (2004).
4. V. Morozov, V. Sizyuk, A. Hassanein, and V. Tolkach, "Simulation of discharge produced plasma and EUV radiation in various Z-pinch devices," ANL Report ANL-ET-04/31, Argonne National Laboratory, Argonne, IL (2004).
5. K. Takenoshita, C.S. Koay, S. Teerawattansook, M. Richardson, and V. Bakshi, "Ion emission characterization from microscopic laser-plasma Sn-doped droplet sources," 3rd Intl. Extreme Ultraviolet Symp. 1-4 November, Miyazaki, Japan (2004).
6. D. Ruzic, D. Alman, K. Thompson, E. Antosen, J. Spencer, and B. Jurczyk, "Measurement and modeling of energetic ions from a commercial EUV Z-pinch," *6th Intl. Conf. Dense Z-Pinches*, Oxford, UK, July, 26, 2005.
7. N. A. Fux, *The Aerosol Mechanic*, Akademia Nauk, Moskow (1955) (in Russian).
8. H. A. Bender, D. O'Connell, and W. T. Silfvast, "Velocity characterization of particulate debris from laser-produced plasmas used for extreme ultraviolet lithography," *Appl. Opt.* **34**, 6513 (1995).
9. V. Banine, "Extreme ultraviolet sources for lithography applications," *3rd International EUVL Symp.*, Miyazaki, Japan (2004).
10. C. Robles, J. Mora, and A. Canals, "Experimental evaluation of the Nukiyama-Tanasawa equation for pneumatically generated aerosols used in flame atomic spectrometry," *Appl. Spectrosc.* **46**, 669 (1992).
11. E. Stadlober and H. Zechner, "The patchwork rejection technique for sampling from unimodal distributions," *ACM Trans. Model. Comput. Simul.* **9**, 59 (1999).
12. B. B. Kadomtsev, "About the active field in plasma," *JETP* **33**, 151 (1957) (in Russian).
13. A. M. Kolchuzhkin and V. V. Uchaikin, *Introduction in Theory of Particles Transmission through Matter*, Amotizdat, Moscow (1978) (in Russian).
14. T. A. Mehlhorn, "A finite material temperature model for ion energy deposition in ion-driven inertial confinement fusion targets," *J. Appl. Phys.* **52**, 6522 (1981).
15. A. F. Akkerman, *Modeling of Charged Particle Trajectories in a Matter*, Energoatomizdat, Moscow (1991) (in Russian).
16. D. C. Ingram and J. A. Baker, "Range distributions of MeV implants in silicon," *Nucl. Instrum. Methods Phys. Res. B* **B7/8**, 361–365 (1985).
17. M. Posselt and W. Scorupa, "The electronic stopping and range profile calculations for high energy implantation of phosphorous into silicon," *Nucl. Instrum. Methods Phys. Res. B* **B21**, 8–13 (1987).
18. V. Sizyuk and A. Hassanein, "Hydrodynamic phenomena of gas-filled chamber due to target implosion in fusion reactors," ANL Report ANL-ET/02-26, Argonne National Laboratory, Argonne, IL (2002).
19. Center for X-Ray Optics Lawrence Berkley National Laboratory (LBNL): See http://www.cxro.lbl.gov/optical_constants/

Biographies and photographs of the authors not available.